Bred Vector and ENSO Predictability in a Hybrid Coupled Model during the Period 1881–2000

YOUMIN TANG AND ZIWANG DENG

Environmental Science and Engineering, University of Northern British Columbia, Prince George, British Columbia, Canada

(Manuscript received 27 October 2009, in final form 2 July 2010)

ABSTRACT

In this study, a breeding analysis was conducted for a hybrid coupled El Niño–Southern Oscillation (ENSO) model that assimilated a historic dataset of sea surface temperature (SST) for the 120 yr between 1881 and 2000. Meanwhile, retrospective ENSO forecasts were performed for the same period. For a given initial state, 15 bred vectors (BVs) of both SST and upper-ocean heat content (HC) were derived. It was found that the average structure of the 15 BVs was insensitive to the initial states and independent of season and ENSO phase. The average structure of the BVs shared many features already seen in both the final patterns of leading singular vectors and the ENSO BVs of other models. However, individual BV patterns were quite different from case to case. The BV rate (the average cumulative growth rate of BVs) varied seasonally, and the maximum value appeared at the time when the model ran through the boreal spring and summer. It was also sensitive to the strength of the ENSO signal (i.e., the stronger ENSO signal, the smaller the BV rate).

Furthermore, ENSO predictability was explored using BV analysis. Emphasis was placed on the relationship between BVs, which are able to characterize potential predictability without requiring observations, and actual prediction skills, which make use of real observations. The results showed that the relative entropy, defined using breeding vectors, was a good measure of potential predictability. Large relative entropy often leads to a good prediction skill; however, when the relative entropy was small, the prediction skill seemed much more variable. At decadal/interdecadal scales, the variations in prediction skills correlated with relative entropy.

1. Introduction

Intensive research has been focused on studying predictability, including potential predictability and actual prediction skill, by examining the perturbation growth. Currently, there are two methods, the singular vector (SV) and the bred vector (BV), which are widely used to analyze the optimal perturbation growth. The earliest work on SVs can be found in Lorenz's (1965) paper, which introduced SVs into meteorology for atmospheric predictability studies. However, SV analysis was not used to investigate ENSO predictability until the late 1990s. Recently, a number of studies on ENSO predictability have used SVs (e.g., Xue et al. 1997a,b; Chen et al. 1997; Thompson 1998; Moore and Kleeman 1996, 1997a,b; Fan et al. 2000; Tang et al. 2006; Zhou et al. 2007).

The breeding method was originally developed to "bred" growing modes related to synoptic baroclinic instability for short-to-medium-range atmospheric ensemble forecasting by taking advantage of the fact that small-amplitude, but faster-growing, convective instabilities saturate earlier. It was first proposed in the 1990s by Toth and Kalnay (1993, 1997). Breeding vectors are, by construction, closely related to Lynapunov vectors (LVs). While BVs have been widely used in mesoscale and synoptic-scale predictions (e.g., Corazza et al. 2003; Kalnay 2003; Young and Read 2008), they have rarely been applied to climate predictions. Cai et al. (2003, hereafter CKT03) first applied the breeding method to the Zebiak and Cane (ZC) (1987) ENSO model, and investigated features of the ENSO BV modes and the potential of BVs for use in data assimilation and ensemble prediction. Yang et al. (2006, hereafter Y06) explored the possibility of separating ENSO-related coupled variability from weather modes and other shorter-time-scale oceanic instabilities using the breeding technique with a fully coupled general circulation model (GCM). Some

Corresponding author address: Youmin Tang, Environmental Science and Engineering, University of Northern British Columbia, 3333 University Way, Prince George, BC V2N 4Z9, Canada. E-mail: ytang@unbc.ca

DOI: 10.1175/2010JCLI3491.1

important properties of ENSO BVs were discovered in CKT03 and Y06, including the relationship of BVs to the ENSO background. They also found that a BV pattern is very similar to the final pattern of the singular vector of the same coupled model.

Several issues of ENSO BVs still warrant further exploration. First, both CKT03 and Y06 used model integration as the reference trajectory (i.e., the initial state) from which a BV is calculated. They performed BV analysis continuously during the period of interest from the beginning to the end. It is also interesting to explore ENSO BVs by using the actual ENSO evolutions as the reference trajectories, which reveals the properties and features of ENSO BVs based on realistic ENSO backgrounds. In particular, the realistic reference trajectory allows for the exploration of the relationship between BVs, which characterize potential predictability without requiring observations, and actual prediction skills, which make use of real observations. Second, it is well known that ENSO predictability has a striking decadal/interdecadal variation (e.g., Chen et al. 2004; Deng and Tang 2009; Tang et al. 2008a). One might be able to shed some light on the mechanism of this decadal/interdecadal variation in ENSO predictability by examining temporal variations in potential predictability, measured by the BV rate or other BV derivatives. In addition, CKT03 and Y06 used, respectively, an intermediate coupled model and a fully coupled GCM for ENSO BV analysis. Applying the breeding method into a hybrid coupled model facilitates ENSO BV analysis for a full spectrum of models.

Considering the use of the breeding method in a hybrid coupled model for the above goals, the period of BV analysis with a realistic ENSO background should be long enough to cover sufficient ENSO cycles, allowing statistically robust conclusions to be drawn. In addition, a long-term retrospective ENSO prediction is required, in order to examine the relationship between BVs and actual prediction skill. The relationship between potential predictability and actual prediction skills has a practical significance, and may offer a means of estimating the confidence that we can place in predictions of the future using the same climate model.

This study pursues the aforementioned objectives. We recently reconstructed the surface wind stress of the tropical Pacific back to 1881 using statistical techniques and using a historic SST and sea level pressure datasets (Deng and Tang 2009). The reconstructed wind stress was applied to a hybrid coupled model to perform retrospective ENSO predictions from 1881 to 2000 (Deng and Tang 2009; Tang et al. 2008a). We also completed the assimilation of a long-term historic SST dataset into an oceanic general circulation model (OGCM) that generated skillful retrospective predictions (Deng et al. 2008). These steps made it possible to implement BVs with realistic ENSO backgrounds over a long period and to explore the relationship between BVs and predictability. This paper is structured as follows: the model and breeding method are introduced in section 2; the results on ENSO breeding modes and optimal error growth rates are presented in section 3; in section 4, the association between the features of BVs and ENSO predictability is explored—especially the measurement of potential predictability based on BVs; finally, the discussion and conclusions can be found in section 5.

2. Model and breeding method

a. Model

A hybrid coupled model (HCM) that was composed of an OGCM coupled to a linear statistical atmospheric model was used for this study. The OGCM was the latest version of the Nucleus for European Modeling of the Ocean (NEMO), identical to the OGCM used in Tang et al. (2008a) and Deng and Tang (2009). (Details of the ocean model are available at http://www.lodyc.jussieu.fr/NEMO/.) The domain of the model used here is configured for the tropical Pacific Ocean from 30°N to 30°S and 122°E to 70°W, with horizontal resolution 2.0° in the zonal direction and 0.5° within 5° of the equator, smoothly increasing to 2.0° at 30°N and 30°S in the meridional direction. There were 31 vertical levels with 17 concentrated in the top 250 m of the ocean. The time step of integration was 1.5 h and all boundaries were closed, with no-slip conditions. The statistical atmospheric model in the HCM was a linear model that predicted the contemporaneous surface wind stress anomalies from SST anomalies (SSTA), which are constructed by the singular vector decomposition (SVD) method with a cross-validation scheme. During the initialization of the hybrid coupled model, the OGCM was forced by the sum of the associated wind anomalies computed from the atmospheric model and the observed monthly mean climatological wind stress. Full details of the model are given in Deng et al. (2008) and Tang et al. (2005, 2008a).

To perform long-term hindcasts with the HCM, past wind stress data are required to initialize forecasts. Using SST as a predictor, as well as SVD techniques, we reconstructed a wind stress dataset back to 1881 (Deng and Tang 2009). The SST data came from the monthly extended global SST (ERSST) dataset from 1881 to 2000 reconstructed by Smith and Reynolds (2004), and had 2° latitude by 2° longitude resolution. The surface wind data came from the monthly National Centers for Environmental Prediction–National Center for Atmospheric

Research (NCEP–NCAR) reanalysis dataset from 1948 to 2000. The data domains for both SST and wind were configured to the tropical Pacific Ocean. The reconstructed wind data has been used to study ENSO predictability (e.g., Tang et al. 2008a; Deng and Tang 2009). The reconstructed winds were assimilated with SST and the HCM to produce the initial conditions of predictions using an ensemble Kalman filter (EnKF; Deng et al. 2008). The retrospective forecasts for the period from 1881 to 2000 were analyzed in detail in Tang et al. (2008a).

b. Breeding analysis

In this study, we derived a BV using the two-sided self-breeding algorithm. The nonlinear model is denoted by M; X indicates the model states that are perturbed for the BV. The BV at step $k + 1$ can be obtained from the below equations, as schematically described by Fig. 1:

$$\mathrm{BV}_{k+1} = \Delta X^{-}_{k+1}, \tag{1}$$

$$\Delta X^{-}_{k+1} = \frac{1}{2}\left[\int_{t_k}^{t_k+\tau} M(X_k + \Delta X^{+}_k)\,dt - \int_{t_k}^{t_k+\tau} M(X_k - \Delta X^{+}_k)\,dt\right], \tag{2}$$

$$\Delta X^{+}_{k+1} = \frac{\Delta X^{-}_{k+1}}{\lambda_{k+1}}, \quad \text{and} \tag{3}$$

$$\lambda_{k+1} = \frac{B^{-}_{k+1}}{B^{+}_{k}}, \tag{4}$$

where $k = 0, 1, \ldots, N$. The number N is the last rescaling step. The term λ_{k+1} is the rescaling factor at step $k + 1$, which is defined by the amplitude of the perturbation growth of the upper-ocean 250-m heat content (HC) over the region of Niño-3.4 (5°N–5°S, 170°–120°W). The upper HC was chosen here because of its critical importance in ENSO simulation and prediction (e.g., Tang 2002). However CKT03 found that a BV is, in fact, relatively insensitive to the definition of the rescaling norm.

The variables B^{-}_{k+1} and B^{+}_{k} in (4) are the spatially averaged amplitude of $\Delta\mathrm{HC}^{-}_{k+1}$ and $\Delta\mathrm{HC}^{+}_{k}$ of the upper-ocean 250-m HC over the domain of Niño-3.4, respectively. Note that the HC is only a model diagnostic variable, thus $\Delta\mathrm{HC}^{-}_{k+1}$ is obtained using the HC definition and (2). In this model, the upper 250 m is covered by the first 17 layers, and the HC is defined as below

$$\mathrm{HC} = \frac{\sum_{i=1}^{17} T_i h_i}{\sum_{i=1}^{17} h_i}, \tag{5}$$

where T_i and h_i are the temperature and thickness, respectively, of the ith model layer obtained by the model integration [i.e., the first or second item of rhs of (2)] and the model initial configuration in vertical, respectively. If we denote ΔHC by the one-dimensional vector $\Delta\mathrm{hc}(i)$, $i = 1, 2, \ldots, \mathrm{N1}$, where N1 is the number of model grids over Niño-3.4 region, we have

$$B^{-}_{k+1} = \sqrt{\frac{1}{\mathrm{N1}}\sum_{i=1}^{\mathrm{N1}} \Delta\mathrm{hc}^2(i)^{-}_{k+1}} \quad \text{and} \tag{6}$$

$$B^{+}_{k} = \sqrt{\frac{1}{\mathrm{N1}}\sum_{i=1}^{\mathrm{N1}} \Delta\mathrm{hc}^2(i)^{+}_{k}}. \tag{7}$$

Initially, $k = 0$, ΔX^{+}_0 is the initial random perturbation x, and B^{+}_0 is the amplitude of initial perturbation x. The term τ is called the rescaling interval. One round of process from k to $k + 1$ is called one breeding cycle, or a rescaling step. A steady BV is obtained after a fast growth of dominant instabilities is saturated (e.g., the BVs after $K + L$ in Fig. 1a).

There are two important parameters in deriving a BV: the initial perturbation amplitude and τ. The initial perturbation magnitude for this study was randomly drawn from a normal distribution with a mean of zero and a variance of a specified value that was 10% of the variance of the model heat content anomalies of the upper ocean 250-m HC, that is,

$$B^{+}_0 \sim N[0, 0.1\sigma(\mathrm{HC})], \tag{8}$$

where σ(HC) is the spatially averaged variance of HC over the region of Niño-3.4, which was obtained from the model control run from 1961 to 2000. Thus, the initial perturbation field $\mathbf{x}$ is determined by

$$\mathbf{x} = B^{+}_0 \mathbf{V}. \tag{9}$$

The matrix $\mathbf{V}$ is the normalized pseudo-Gaussian noise field with spatial coherence, given by Evensen (2003), which has been widely used in ensemble Kalman filter. Several sensitivity experiments show that, when using this setting for the initial perturbation, the perturbed solution quickly diverges from the control solution after one rescaling step and meanwhile, the breeding vectors can converge in four–six rescaling steps, as shown in Fig. 2.

The rescaling interval is a little arbitrary. Peña and Kalnay (2004) argued that this period should be longer than two weeks for slowly varying coupled instability. CKT03 used three months to obtain bred vectors for the ZC model whereas Y06 used one month for a coupled

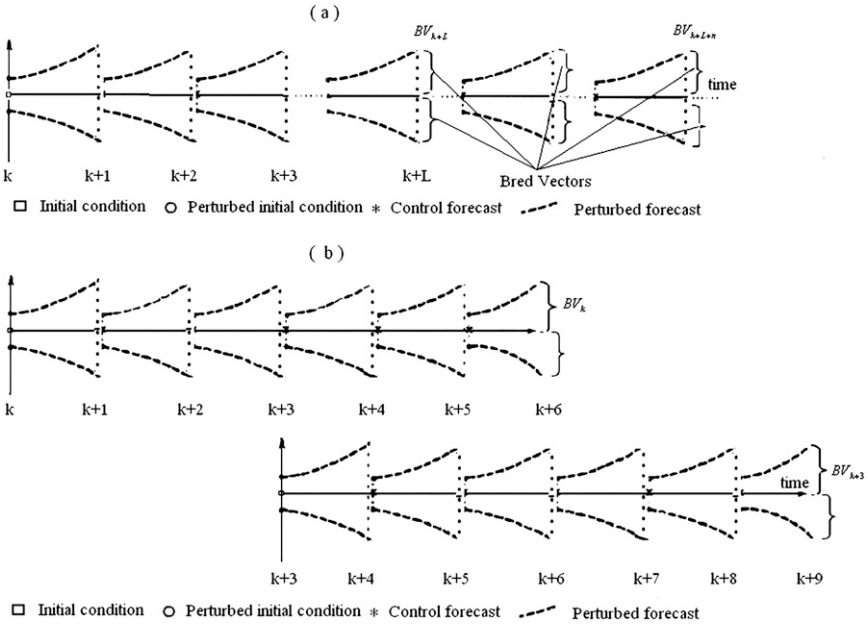

FIG. 1. A schematic of the two-sided self-breeding BV algorithm. (a) The steady BVs were obtained only after a few rescaling steps (i.e., $K + L$) and the unperturbed model forecast was always used as a reference trajectory for each BV. (b) Each BV was derived from a realistic initial condition and obtained by six rescaling steps (see text). The interval between two rescaling steps (e.g., k to $k + 1$) was 1 month. In this study, the BV was analyzed every 3 months from January 1881 to October 2000 using (b).

global general circulation model. In this study, we choose a rescaling period of one month, which leads to the saturation of fast growing instabilities after four–six rescaling steps, as discussed in the next section.

To provide a sufficient sample of the dynamically important uncertainties of the initial state, we used 15 pairs of random perturbations for each initial condition (i.e., obtaining 15 BVs). The perturbed variables included the sea temperature, horizontal currents, and vertical currents of the top 250 m (17 model levels).[1] The BVs were computed at 3-month intervals from January 1881 to October 2000 (i.e., January 1881, 1 April 1881, ... October 2000). Thus there are a total of 15 × 480 BVs for each variable of interest during the entire period, providing sufficient sampling to conduct robust statistical analyses. The corresponding time for each BV was the initial time from which the random initial perturbation was added to the model state (see Fig. 1b).

It should be mentioned that the above BV approach is different from that used in CKT03 and Y06 because they analyzed BV cycles continuously until the end of the entire period, as demonstrated in Fig. 1a. The essential difference between our approach and theirs is the initial perturbation and initial condition used to generate the BV. In their approach, the rescaling is done continuously until the end. The initial perturbation for the next BV was always the previous BV, and was imposed onto unperturbed forecasts, ensuring the fast growth of instabilities to be saturated in one rescaling step after a period of initial training (e.g., beyond $K + L$ in Fig. 1a). It is similar to the method of Toth and Kalnay (1993) where the previous BV was centered around the evolving analysis state for the next BV. A common feature of CKT03, Y06, and Toth and Kalnay (1993) is that the analysis state (or unperturbed forecast) and BV analysis are for the same model. However, the analysis state in this work is from an ocean data assimilation system that is different from the coupled model used for BV analysis; thus, inconsistencies exist between modeling system for the BV cycle and the modeling system for oceanic analyses, leading to an initial shock in performing BV of each initial condition. Thus, our approach always takes a complete BV analysis from a random initial perturbation to the saturation of the fast

[1] Considering the computational expense in preparing initial perturbations, we did not perturb all model variables. The choice of temperature and currents as the variables that were perturbed was due primarily to their significant importance in ENSO formulation and development although it was a somewhat arbitrary. The top 250 m cover the thermocline in the equator, which dominates ENSO variability.

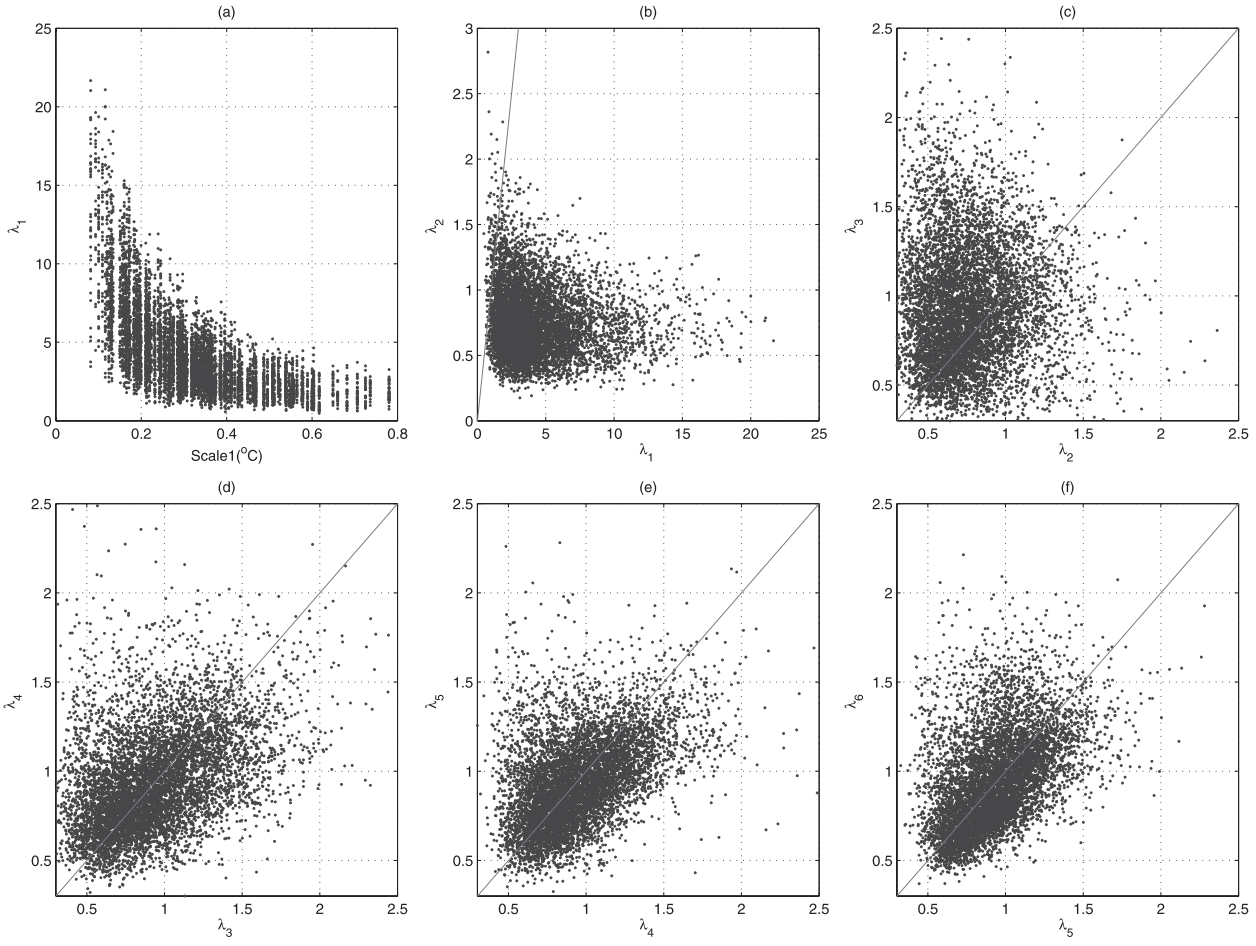

FIG. 2. Scatterplots of λ of two adjacent breeding cycles for all of the perturbations during the entire period from 1881 to 2000. The lines in (b)–(f) indicate $\lambda_{k-1}^{\mathbf{m}} = \lambda_k^{\mathbf{m}}$. Note that the x axis is different between (a) and the other panels. The initial perturbation grows very quickly at the first rescaling step (Fig. 2a) due to the fast growth of nonlinear instabilities; however, the growth rate varies little after four rescaling steps, indicating a gradual saturation of the growth of nonlinear instabilities.

growth of instabilities for each analysis state (Fig. 1b). Sensitivity experiments indicate that such a complete BV analysis usually takes four to six rescaling steps for the HCM that has a noise-free atmospheric component. Such an approach also allows us to analyze the BV of each initial condition in a completely parallel manner. In concept, our approaches is the same as that of Toth and Kalnay (1993), including its definition of a BV, although it is more expensive. We used a realistic analysis state, rather than an unperturbed forecast, as the initial condition of each BV because we wanted to explore perturbation growth under a realistic ENSO background, in addition to the relationship between BV s and prediction skills. In fact, our approach is very similar to the singular vector analysis for each initial condition that was performed by Lorenz (1965) using a linear tangent model.

To measure the perturbation growth from the initial time until the saturation of fast-growing instabilities, a cumulative growth factor for breeding vector **m** after step k was defined, as described in Young and Read (2008):

$$G_k^{\mathbf{m}} = \begin{cases} \lambda_1^{\mathbf{m}} & \text{if} \quad k = 1; \\ \lambda_k^{\mathbf{m}} G_{k-1}^{\mathbf{m}} & \text{if} \quad k > 1. \end{cases}$$

The term $G_k^{\mathbf{m}}$ is λ_k multiplied by the previous cumulative growth rate. A cumulative growth factor may better characterize potential predictability because the prediction errors at leading times of k steps depend on the error growth not only from $k-1$ to k, but also from the initial time to $k-1$.

The averaged $G_6^{\mathbf{m}}$ over 15 BVs is denoted by G_6, namely,

$$G_6 = \frac{1}{15} \sum_{\mathbf{m}=1}^{15} G_6^{\mathbf{m}}. \tag{10}$$

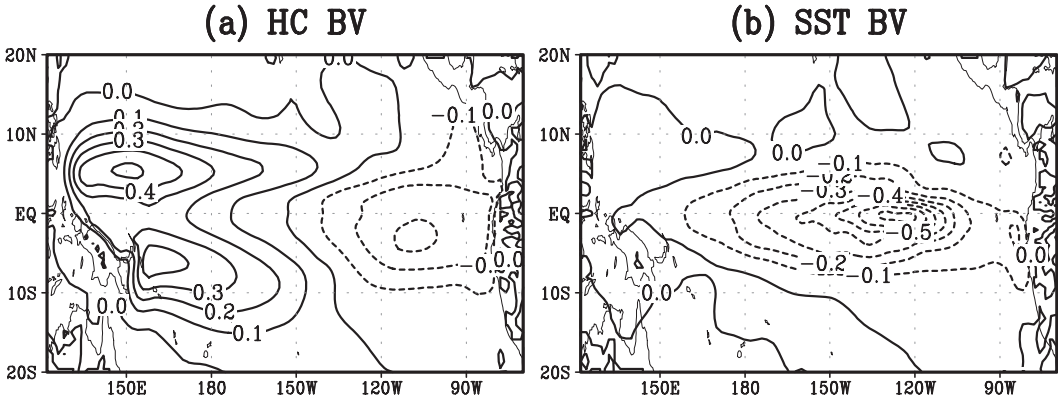

FIG. 3. The first EOF modes of (a) HC and (b) SST. The EOF analysis was employed using all bred vectors from 1881 to 2000. The first modes explain 70% and 61% of the total variance for HC and SST, respectively. The units are °C.

The term G_6 is referred to as the BV rate, the average growth rate of bred vectors associated with a given initial state. In total, there are 480 G_6 here during the period from 1881 to 2000.

3. ENSO BVs and BV rate

In this section, preliminary features of ENSO bred modes and their variations with initial state, season, and ENSO signal are explored. The required number of rescaling steps depends on model dynamics, initial state, initial perturbation, and other factors. In sensitivity experiments, we found that the fast unstable growth was saturated after four to six rescaling steps in the HCM. The scatter-space plot of λ of two subsequent rescaling steps for all of the BVs for the entire period from 1881 to 2000 is shown in Fig. 2. As can be seen in this figure, the initial perturbation grows very quickly at the first rescaling step (Fig. 2a) because of the fast growth of nonlinear instabilities. However the growth rate varies little after four rescaling steps, indicating a gradual saturation of the growth of nonlinear instabilities. Thus, we focused on the BVs of the sixth rescaling step in this study. Unless otherwise indicated, all of the results of BVs presented in this paper are from the sixth rescaling step with the exception of the BV rate that is the cumulative growth rate from rescaling steps 1–6 as defined above.

a. ENSO bred modes

Figure 3 shows the first EOF modes of BVs for SST and HC obtained using all of the BVs from 1881 to 2000 (i.e., 480 × 15 BVs), accounting for 61% and 70% of the total variance, respectively. The first modes, denoted by $\mathrm{EOF}_{\mathrm{total}}$, describe a classic ENSO-like structure. Figure 3a for HC has a dipole zonal structure suggesting a western Pacific ''Rossby wave–like'' response of one sign and an eastern Pacific ''Kelvin wave–like'' response of the opposite sign (e.g., Tang 2002). Figure 3b for SST has a large-amplitude signal of one sign located primarily in the equatorial central and eastern Pacific. These patterns agree with the idea of a heat content buildup prior to an El Niño as postulated by Jin (1997), and the delayed oscillator mechanism (Battisti 1988; Suarez and Schopf 1988); the patterns are also similar to the BVs from the fully coupled NCEP and the National Aeronautics and Space Administration (NASA) Seasonal-to-Interannual Prediction Project (NSIPP) GCMs reported in Y06.

When compared with leading singular vectors in many ENSO models, the patterns in Fig. 3 resemble their final patterns (e.g., Chen et al. 1997; Xue et al. 1997a; Zhou et al. 2007; Cheng et al. 2010, hereafter C10). Similarities between BVs and the final patterns of SVs were also noticed in CKT03 and Y06.

It has been found in previous work that the SVs are insensitive to initial conditions in many models (e.g., Chen et al. 1997; Xue et al. 1997a; Zhou et al. 2007; C10). To explore the sensitivity of BV to initial conditions, we calculated the spatial correlation R_{space} between EOF_i, the first EOF mode obtained using 15 BVs for the ith initial condition ($i = 1, 2, \ldots, 480$), and $\mathrm{EOF}_{\mathrm{total}}$, shown by Fig. 3. If the $\mathrm{EOF}_{\mathrm{total}}$ and the EOF_i are denoted by the normalized one-dimensional vectors $\mathbf{eof}_{\mathrm{total}}$ and $\mathbf{eof}_i$, respectively, the spatial correlation is calculated as follows:

$$R^i_{\mathrm{space}} = \frac{1}{\mathrm{NP}-1}\sum_{p=1}^{\mathrm{NP}} \mathbf{eof}_{\mathrm{total}}(p)\mathbf{eof}_i(p), \qquad (11)$$

where NP is the number of total model grids over the model domain, and $i = 1, 2, \ldots, 480$.

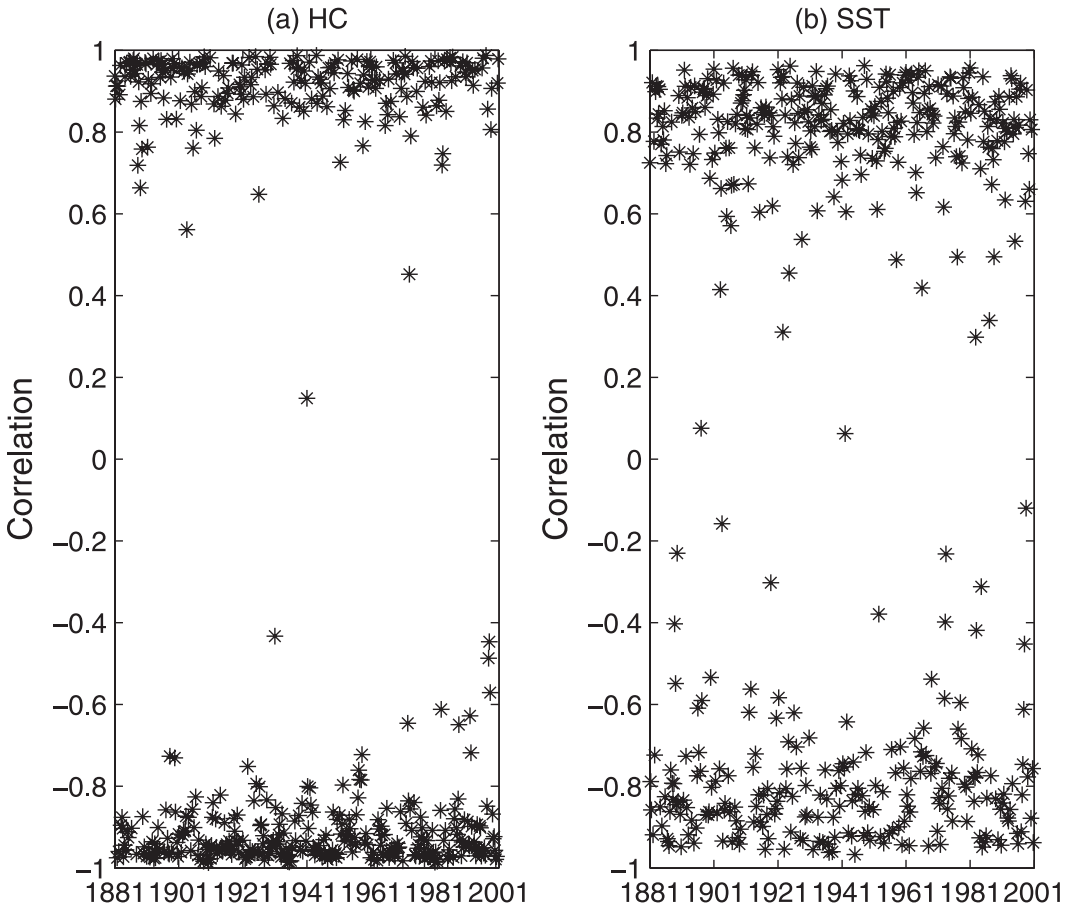

FIG. 4. The spatial correlation between EOF_{total} and EOF_i, where EOF_{total} is the first EOF mode obtained using all BV vectors (480×15), whereas EOF_i is the first EOF mode obtained using 15 BVs for the initial condition i ($i = 1, 2, \ldots, 480$).

The spatial correlation measures the similarity between the dominant direction in the space spanned by BVs at different time instances and the dominant direction in the space spanned by BVs computed over a long time period. The result is shown in Fig. 4. For most cases (over 90%), the absolute value of the spatial correlation coefficient is over 0.90, with an overall average value above 0.85 for all cases for both HC and SST. As argued by CKT03, the positive phase of the same pattern should be regarded as equivalent to the negative phase, at least from a linear system perspective. In addition, the pattern sign can be arbitrary from the view of EOF analysis. We also performed bootstrap experiments [i.e., randomly choose two initial conditions (among 480)], and the spatial correlation of the leading EOF mode was calculated between the two initial conditions [i.e., $\mathbf{eof}_j$ instead of $\mathbf{eof}_{total}$ in (11)]. The process was repeated 1000 times. The results showed that 70% and 93% of the absolute values of the correlation coefficient were over 0.65^2 for SST and HC, respectively. Thus, the preliminary features of BVs, as represented by the first EOF mode (equivalent to the average), are not highly sensitive to initial conditions. This conclusion is further confirmed by Fig. 5, the pattern of the first EOF modes obtained using all of the BVs in four different calendar months, indicating the seasonal independence of the BVs.

The above finding on the insensitivity of BVs to initial conditions results from the similarity of the EOF-characterized dominant structure in the space spanned by the BVs of different initial conditions. Further examination was conducted on individual BVs at different initial conditions. In other words, is an individual BV at the

[2] The value of 0.65 was chosen arbitrarily, a very large value compared with the threshold value of statistical significance at the confidence level of 99%.

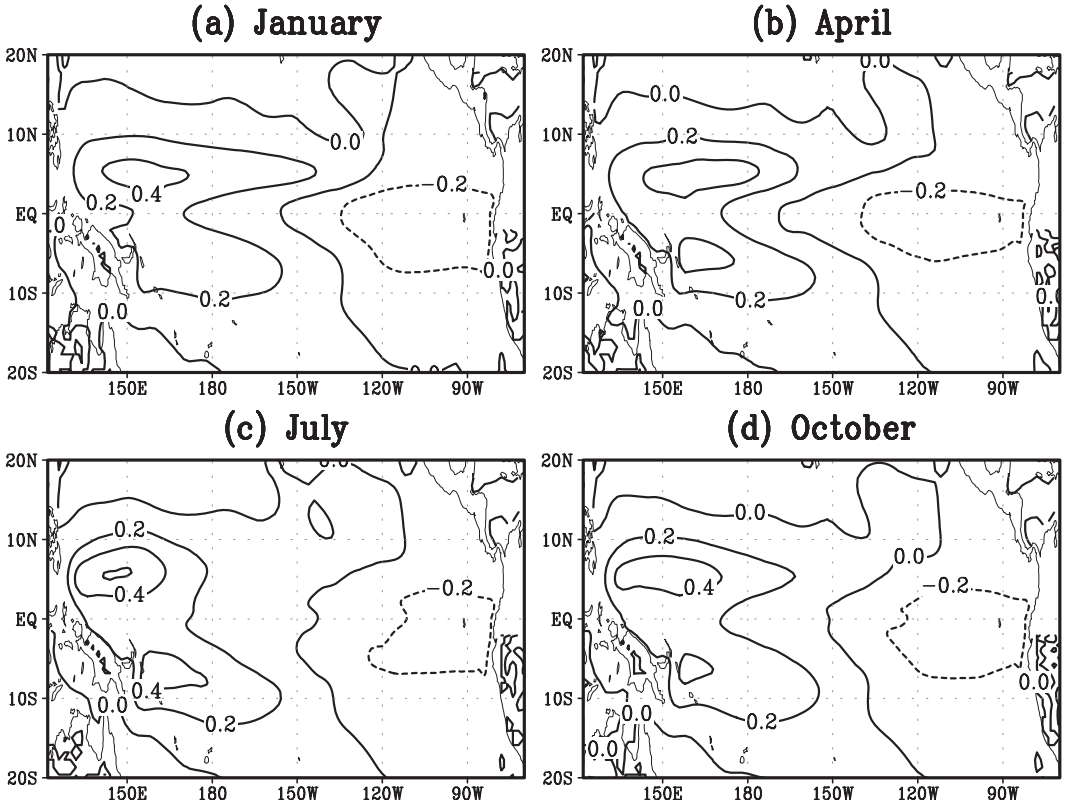

FIG. 5. The first EOF mode of HC obtained using all of the BVs of four different calendar months.

initial time t_1 similar to another BV at its initial time t_2? To explore this question, we randomly chose two individual BVs at two different initial conditions and calculated their spatial correlation coefficient. This process was repeated 1000 times, as shown in Fig. 6. The correlation coefficients are almost evenly distributed across the range from the maximum (1) to the minimum (−1), indicating that an individual BV is dependent on its initial conditions.

The average of the ensemble BVs had a stable structure independent of the initial state whereas the individual member of ensemble BVs was sensitive to the initial state. One physical interpretation for this is that the mean of ensemble BVs is probably dominated by time-independent model dynamics (e.g., the delayed-oscillator mechanism), whereas the individual BV member is greatly impacted by an initial random perturbation. In Toth and Kalnay's approach, the initial perturbation came from multiple modes orthogonalizing in various ways that were not completely random in nature; thus, the BV derived from their approach is probably equivalent to the mean of the ensemble of BVs here.

b. Variations of BV rate

The BV rate G_6, defined in section 2b, measures the mean growth rate of all of the BVs for a given initial state. Shown in Fig. 7 is the average G_6 of all of the BVs for four different calendar months. As can be seen, the greatest BV rates occur in January and April, during which the model runs through the boreal spring and summer (because of the 6 rescaling steps for each BV, equivalent to 6 months). This is in good agreement with the variation of the optimal error growth rate in the ZC model (e.g., CKT03; C10). The seasonal dependence of error growth might explain why ENSO prediction skill often drops remarkably when predictions go through the spring (i.e., the "spring barrier"). This increase in error is due to the fact that the intertropical convergence zone (ITCZ) is closest to the equator during the spring, sustaining unstable conditions and enhancing convective instability. In contrast, the ocean–atmosphere interaction is strong during the summer due to the relatively large vertical temperature gradient and ocean upwelling (e.g., Xue et al. 1997a), which lead to strong baroclinic instability.

Because of the existence of decadal/interdecadal variations in ENSO variability and prediction skills (e.g., Tang et al. 2008a), it is interesting to examine temporal variations in the BV rate. Figures 8a,b show variations in the BV rate and the Niño-3.4 SSTA index from 1881 to 2000, for which a 2-yr running mean has been applied to

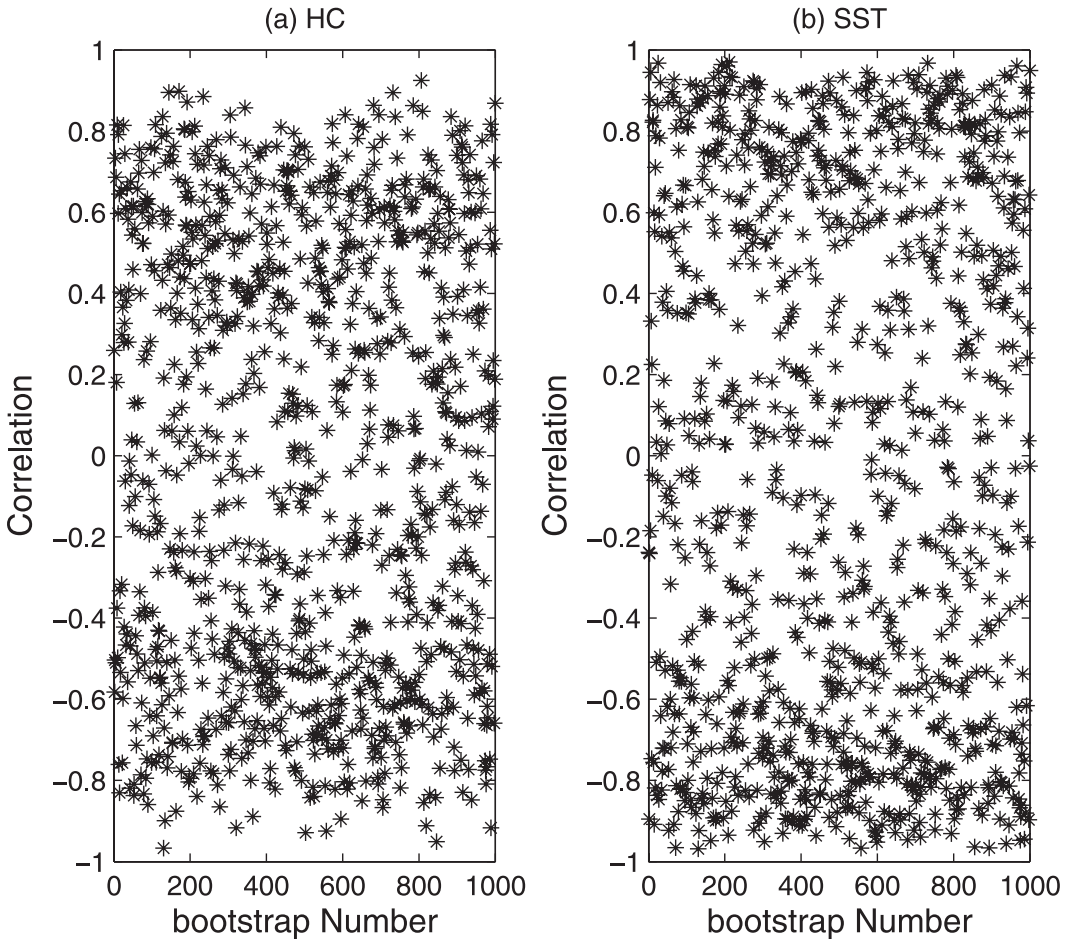

FIG. 6. Correlation between two arbitrary BVs from two arbitrary initial conditions. These arbitrary BVs and initial conditions were randomly chosen, and this process was repeated 1000 times.

address interannual and longer signals. As previously indicated, the interannual variability is obvious in both the BV rate and in the Niño-3.4 SSTA index. Further scrutiny of Figs. 8a,b reveals that the interannual variability of the BV rate has decadal/interdecadal variation. For example, the magnitude of the BV rate is visibly smaller during the 1880s and 1980s than during other periods. The variability of the BV rate at various time scales is more obvious in the wavelet analysis shown in Fig. 8c. The local wavelet power spectrum clearly indicates that significant periods were localized in time and varied from 2 to 16 yr from 1881 to 2000. A striking feature in Figs. 8c,d is the strong interannual variability and relatively weak decadal variability. Comparing Figs. 8c with 8d reveals similar oscillatory characteristics between the BV rate and ENSO variability, suggesting an association of the BV rate with the ENSO background.

The dependence of the growth rate of BVs on the ENSO phase has been addressed in CKT03 and Y06. They found that a large error growth tends to occur in a neutral or onset/breakdown stage of an ENSO event, such as 3–4 months prior to the peak phase, whereas a small error growth often occurs in an ENSO peak phase. In their work, the model integration was used as the reference trajectory for their BV analysis, as mentioned in section 2b. The relationship between the BV rate and ENSO phase was then explored by comparing our BVs with the realistic ENSO evolution as the initial reference trajectory.

Figure 9 shows the average BV rate as a function of ENSO phase. The ENSO events are binned into nine categories based on the Niño-3.4 SSTA index. Three kinds of events, El Niño, La Niña, and neutral events, are explored here. They are classified by Niño-3.4 SSTA index (°C) greater than 2.0, 1.5, and 1.0; less than −2.0, −1.5, and 1.0; and in the range of (−0.5, 0.5), (−0.3, 0.3), and (−0.1, 0.1), respectively. Considering 6 rescaling steps (equivalent to 6 months) for each BV, we selected the BV rate of the 3 months prior to the time when the

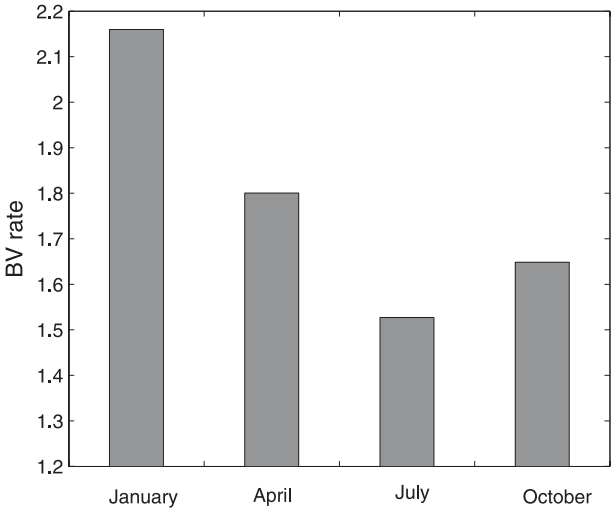

FIG. 7. The average BV rate for all of the initial conditions for January, April, July, and October.

criteria value was met. Thus, the BV rate shown in Fig. 9 actually represents the error growth of a 6-month duration (i.e., 3-month prior to and after the occurrence of an ENSO event). As can be seen in Fig. 9, there was a small error growth rate during the peak ENSO stages (El Niño and La Niña), while a large error growth rate occurred during the neutral stages. The stronger the background SSTA of ENSO, the smaller the BV rate. These results are generally consistent with those in CKT03 and Y06 as well as former SV studies (e.g., Chen et al. 1997; Zhou et al. 2007). Both CKT03 and Zhou et al. 2007 analytically derived this converse relationship between the error growth rate and the ENSO signal by using a delay-oscillator model (Suarez and Schopf 1988). This relationship suggests that a strong ENSO signal tends to reside in a dynamical stable regime, whereas a weak signal is probably more associated with an instable dynamical process. Another possibility is that the model ENSO strength is bounded above so that error growth can take place only in one direction (e.g., neutral phase) when one is near the extreme, resulting in a situation where instability might remain large in the direction toward neutral. In addition, Fig. 9 shows that the BV rate is smaller during El Niño than during La Niña, possibly because the tropical wave instability is more active when the cold tongue is well established in the east (Y06).

The converse relationship between the BV rate and ENSO signal is further demonstrated in Fig. 10, the scatterplot of the BV rate against the ENSO signal. The ENSO signal here is defined by the variance of the observed Niño-3.4 SSTA index, computed using a 20-yr

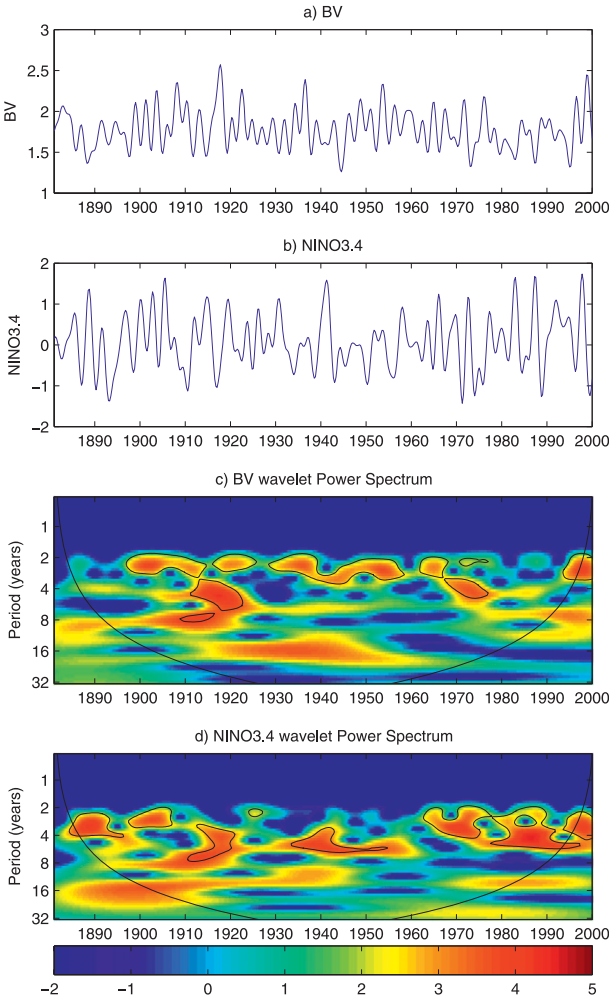

FIG. 8. Variation in (a) the BV rate and (b) the Niño-3.4 SSTA index from 1881 to 2000. The wavelet power spectrum of (c) the BV rate and (d) the Niño-3.4 SSTA using the Morlet wavelet. The thick contour encloses regions of greater than 95% confidence using a red-noise background spectrum. The solid smooth curves in the left and right corners indicate that edge effects become important. The time window used here was $2\sqrt{2}T$, a function of period T.

running window from 1881 to 2000.[3] A strong converse relationship is observed in Fig. 10 with a correlation coefficient of −0.71 between the ENSO signal and the BV rate. A similar result can be obtained using other measures of the ENSO signal, such as the total spectrum power of Niño-3.4 SSTA index at the frequencies of 2–5 yr or the variance explained by the first EOF mode of SSTA (HCA).

[3] The variance obtained during a 20-yr window is plotted at the middle point of the window. For example, the variance at 1890 is calculated using the samples from 1881 to 1900. The 20-yr window is shifted by 3-months each time starting from 1881 to 2000. The BV rate plotted is the average value of BVs of each window.

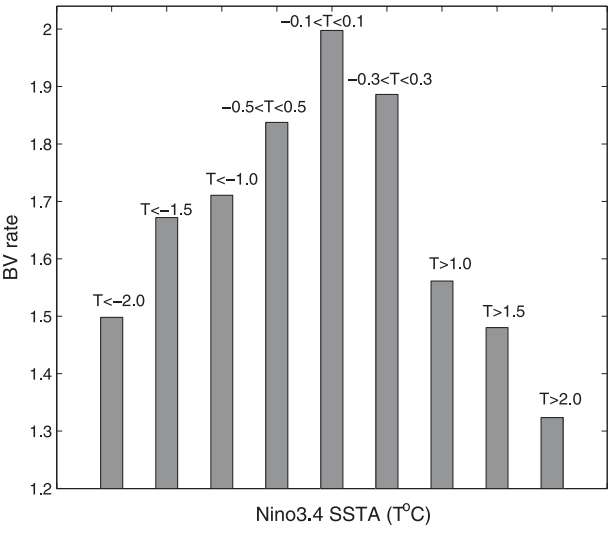

FIG. 9. The average BV rate as a function of the ENSO phase, indicating the error growth rate during La Niña, neutral, and El Niño events. Three kinds of El Niño (La Niña) cases were explored with Niño-3.4 SSTA index greater (less) than 1.0 (−1.0), 1.5 (−1.5), and 2.0 (−2.0), respectively; whereas three kinds of neutral cases were explored using the ranges of Niño-3.4 SSTA index between (−0.5, 0.5), (−0.3, 0.3), and (−0.1, 0.1), respectively.

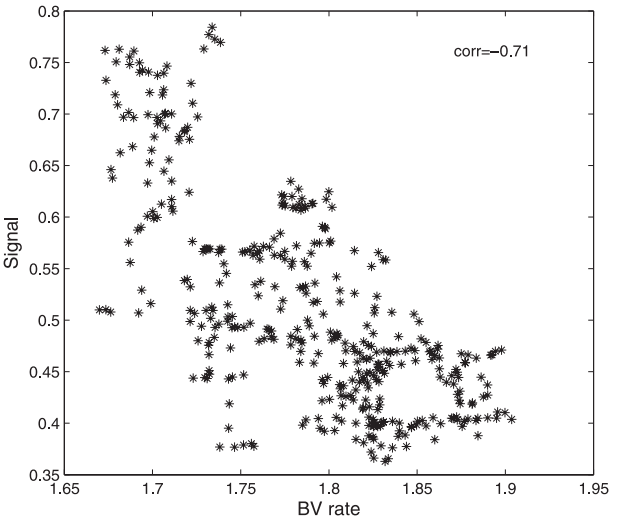

FIG. 10. Scatterplot of the BV rate against the ENSO signal.

4. ENSO predictability

In this section, we will explore ENSO predictability. Emphasis was placed on identifying a measure calculated from BVs that was able to quantify potential predictability and had a relationship with actual prediction skill. This relationship offers a practical means of estimating the confidence level of an ENSO forecast using the HCM.

The retrospective ENSO prediction was performed for the period from 1881 to 2000 using the HCM. A total of 480 forecasts, initialized from January 1881 to October 2000, were run starting at 3-month intervals (1 January, 1 April, 1 July, and 1 October), and continued for 12 months for the HCM. The SST assimilation was performed to initialize the forecasts, as introduced in section 2a.

a. Bred vector and BV rate

Figure 11 shows the average correlation R and RMSE of SSTA predictions against the observed values over lead times of 1–6 months [i.e., $(1/6)\sum_{l=1}^{6} R_l(\mathrm{RMSE}_l)$, where l is the index of lead month] for the period from 1881 to 2000. As indicated, the best correlations occur in the equatorial central and eastern Pacific (as in many ENSO models; e.g., Goddard et al. 2001; Tang et al. 2008a), where there was the largest error growth, as shown in Fig. 3. This seemingly contradicts the widespread perception that good prediction ability should correspond with a small error growth rate (e.g., Farrell 1990; Tang et al. 2008b; Orrell 2003). One probable reason is that error growth, as shown in Fig. 3, can be decomposed into linear growth and nonlinear growth. The linear errors only impact amplitude prediction, whereas nonlinear errors impact phase prediction. Thus, the correlation is still likely to be high if the large error growth rate is due mainly to linear instabilities. Tang and Deng (2010) found that, indeed, the region of high correlation coefficients has relatively weak nonlinearity. This argument is also supported by the fact that the region of good correlations often has a large *RMSE* in ENSO models, as shown in Fig. 11b.

Figure 12 shows the scatterplot of the correlation and the RMSE of individual predictions against the corresponding BV rates using the same initial conditions applied to both the BVs and the predictions. The RMSE/correlation value of individual predictions (RMSEIP/CIP) was used to measure the error (correlation) of an individual forecast for all leads L (=12 months), defined as

$$\mathrm{RMSEIP} = \sqrt{\frac{1}{L-1}\sum_{t=1}^{t=L}[T^p(t) - T^o(t)]^2} \quad \text{and} \tag{12}$$

$$\mathrm{CIP} = \frac{\sum_{t=1}^{L}(T_t^p - \mu^p)(T_t^o - \mu^o)}{\sqrt{\sum_{t=1}^{L}(T_t^p - \mu^p)^2}\sqrt{\sum_{i=1}^{L}(T_t^o - \mu^o)^2}}. \tag{13}$$

Here, T is the index of Niño-3.4 SSTA, p denotes forecasts, o denotes observations, t is the lead time of the forecast, μ^p is the mean of the forecasts, μ^o is the

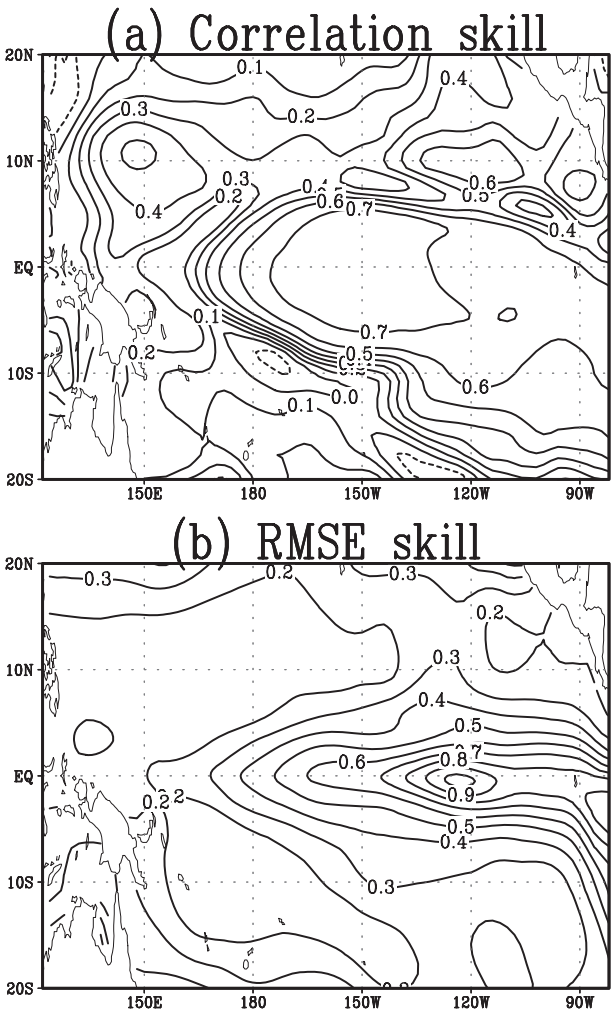

FIG. 11. (a) Correlations and (b) RMSEs of predicted Niño-3.4 SSTA against the observed values for the past 120 yr from 1881 to 2000, averaged over lead times of 1–6 months.

mean of observations, and L is the number of samples used.

Figure 12 includes all of the initial conditions from 1881 to 2000, showing little visible relationship between the BV rate and prediction skill and suggesting that the BV rate probably is not a good measure of potential predictability for this HCM. However, one should take caution when interpreting this figure because of the small sample size used in making this calculation, especially for the correlation coefficient. We next explore the other measure of potential predictability and examine its relationship to prediction skills.

b. Relative entropy derived from BVs

Recently, a new theoretical framework for measuring the uncertainty of predictions has been developed and applied to examine atmospheric and climate potential predictabilities (Schneider and Griffies 1999; Kleeman 2002, 2008; Tippett et al. 2004; Tang et al. 2005, 2008b; DelSole 2004, 2005). The approach is built on information theory (Cover and Thomas 1991). It has been argued that the relative entropy (RE) of an individual prediction, defined as the difference between the climatological probability density function (PDF) and the prediction PDF, is a good measure of its prediction utility. A larger RE indicates that more useful information is being supplied by the prediction, which could be interpreted as making it more reliable.

In the case where the PDFs are Gaussian, which is approximately the case in many practical instances (including ENSO prediction), the relative entropy RE of an individual prediction may be expressed exactly in terms of the prediction variance σ_p^2, evaluated typically by ensemble members, the model climatological variance σ_q^2, obtained from a model climatological run, and the difference $\mu^p - \mu^q$ of the ensemble and the climatological means (Kleeman 2002):

$$\mathrm{RE} = \frac{1}{2}\left[\log\frac{\sigma_q^2}{\sigma_p^2} + \frac{\sigma_p^2}{\sigma_q^2} + \frac{(\mu^p - \mu^q)^2}{\sigma_q^2} - 1\right]. \quad (14)$$

Figure 13 is as in Fig. 12, but using the RE of Niño-3.4 SSTA index instead of the BV rate. Here the climatological variance and mean were obtained from samples of all BVs for all initial conditions from 1881 to 2000 (i.e., 480 × 15 samples), as in Tippett et al. (2004) and Tang et al. (2005). As can be seen in Fig. 13, a large RE often led to a good prediction skill (i.e., a small RMSE and a large correlation); however, when the RE was small, the prediction skill seemed much more variable. This result is very similar to the so-called triangular relationship that has been found to characterize the relationship between ensemble spread and prediction skill in ensemble weather forecast. This finding also resembled the relationship between ensemble signal and prediction skill in ensemble climate prediction (ECP; e.g., Buizza and Palmer 1998; Xue et al. 1997b; Moore and Kleeman 1998; Tang et al. 2008b). For instance, it was found in ECP that, when the ensemble signal is large, the prediction is invariably good; whereas when it is small, the prediction can be much more variable. Thus, we also used the ''triangular relationship'' to describe the relationship between the RE and prediction accuracy in this study. Figure 13 suggests that the RE derived from BVs could be an effective indicator of ENSO prediction skill.

The importance of RE in measuring potential predictability has been addressed in previous studies (e.g., Kleeman 2002, 2008; Tippett et al. 2004; Tang et al. 2005, 2008b), but all of these used prediction ensemble to

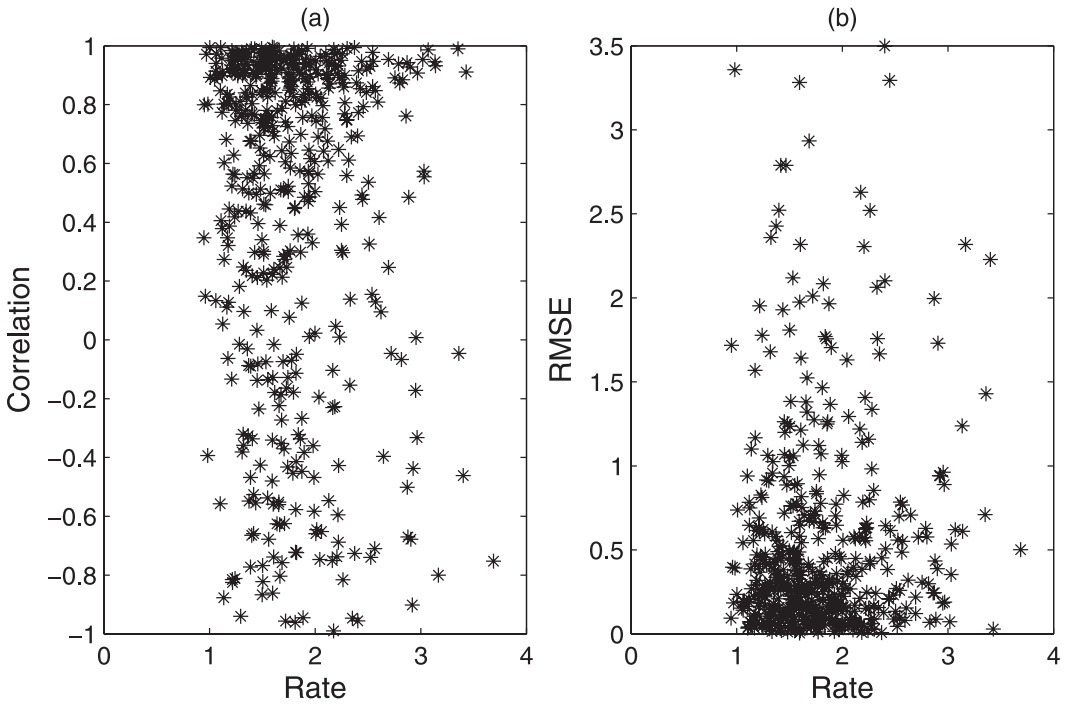

FIG. 12. Scatterplot of (a) correlations and (b) RMSEs of each individual prediction against the BV rate for the corresponding initial condition.

calculate RE. Here we used BVs to calculate RE and obtained similar results. This is probably due to the intrinsic coherence of BVs with ensemble predictions. From the point of calculation expense, the BV-based RE is comparable to the ensemble-prediction-based RE when the BV analysis is incorporated with the ensemble run. However, if the ensemble prediction system is independent to the generation of the optimal perturbation modes (e.g., singular vector), the BV-based RE is much cheaper than the ensemble-prediction-based RE.

c. *Decadal/interdecadal variation in relative entropy and predictability*

In many ENSO models, ENSO predictability clearly has a decadal/interdecadal variation (e.g., Chen et al. 2004; Tang et al. 2008a). It was found that the interdecadal variation in ENSO predictability was in good agreement with the signal of interannual variability and with the degree of asymmetry of an ENSO system (e.g., Tang et al. 2008a; Tang and Deng 2010). Below the relationship between relative entropy and ENSO predictability at decadal/interdecadal time scales is examined.

Figure 14 shows the average R and RMSE values for the Niño-3.4 SSTA index with a 1–12-month lead, measured by a 20-yr running window that moved at 1-yr intervals from 1881 to 2000 (i.e., 1881–1900, 1882–1901, 1883–1902, . . . , 1980–99, 1981–2000), where the predicted Niño-3.4 SSTA is compared against the observed value.[4] The average relative entropy over the running window is also plotted in Fig. 14 (solid line). As can be seen in this figure, the prediction skills show a pronounced interdecadal variation. Generally there was a high prediction skill in the late nineteenth century and in the middle to late twentieth century, and a low skill from 1901 to 1960. Such an interdecadal variation feature was also manifested in the RE. The correlations between the RE and the correlation coefficient and between the RE and the RMSE were 0.76 and −0.66, respectively, thus, the larger the RE, the larger the correlation and the smaller the RMSE.

Further examination of RE might provide some insights into interdecadal variations in ENSO predictability. The first two terms on the right-hand side (rhs) of (14) are determined by the climatological variance and predictive variance. Because variance of climatology is time invariant, these terms represent a measurement of

[4] The average skills, as a function of the index of window, were obtained by $(1/12)\sum_{l=1}^{12} R_l^L(\mathrm{RMSE}_l^L)$, where l is the index of the lead month and L is an index of a 20-yr window that shifts by 1 yr from the beginning to the end during the period from 1881 to 2000 (January 1881, April 1881, . . . , October 2000). The term $R_l^L(\mathrm{RMSE}_l^L)$ is the skill for the window L measured using 20-yr samples, as a function of the lead time l.

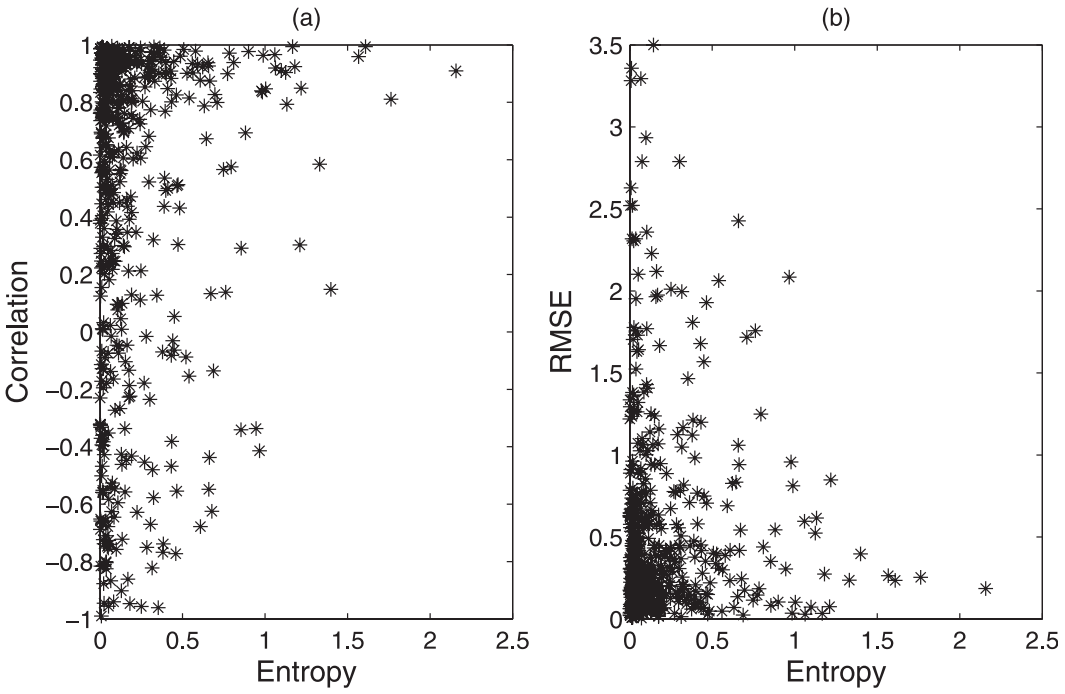

FIG. 13. Scatterplot of (a) correlations and (b) RMSEs of each individual prediction against the relative entropy for the corresponding initial condition.

the dispersion or spread of the BVs. The third term on the rhs of (14) is governed by the amplitude of the mean of the BVs. We refer to the first two terms minus 1 as the dispersion component (DC) and the third term as the signal component (SC).

Figure 15 shows the variations in DC and SC against RE for the period from 1881 to 2000. This figure reveals that DC is significantly larger than SC, and RE is dominated by DC. As can be seen in Fig. 15a, RE and DC vary linearly with a slope of unity. The correlation coefficient between R and DC is 0.97. In contrast to the good relationship between DC and RE, the relation between SC and RE was much less significant. Figure 13 indicates that the triangular relationship between the RE and prediction skill is equivalent to the triangular relationship between ensemble spread and skill that was found in some numerical weather models.

It should be noticed that Fig. 15 differs from an earlier result reported by Tang et al. (2005). They found that the SC plays a dominant role in the RE s for two ENSO models. This is most likely due to disparities with models and methods used in these two cases. In this study, we used a different HCM. In particular, BVs were used to calculate the RE rather than the ensemble prediction itself used in Tang et al. (2005). Figures 15 and 14 indicate a possible mechanism of interdecadal variation in ENSO predictability; namely, when the ENSO cycle resides in a phase that has a relatively large DC, it is more predictable and vice versa.

5. Discussion and summary

The breeding method has been widely applied in a variety of fields including atmospheric and climate predictability, data assimilation, and ensemble prediction.

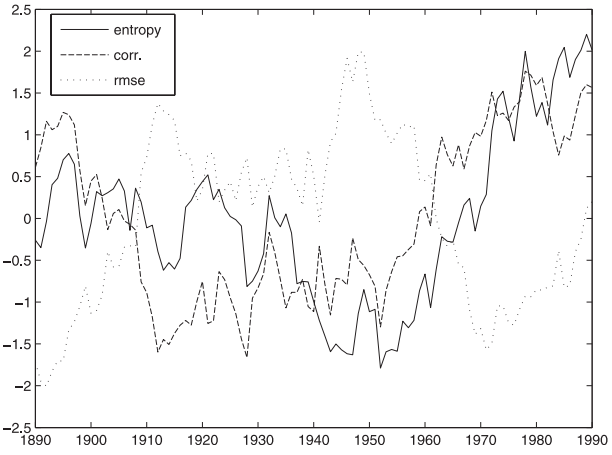

FIG. 14. Variations in the relative entropy (solid), the average correlation coefficient (dashed), and RMSE (dotted) over 1–12-month lead times from 1881 to 1990. Normalization was done for each variable prior to plotting.

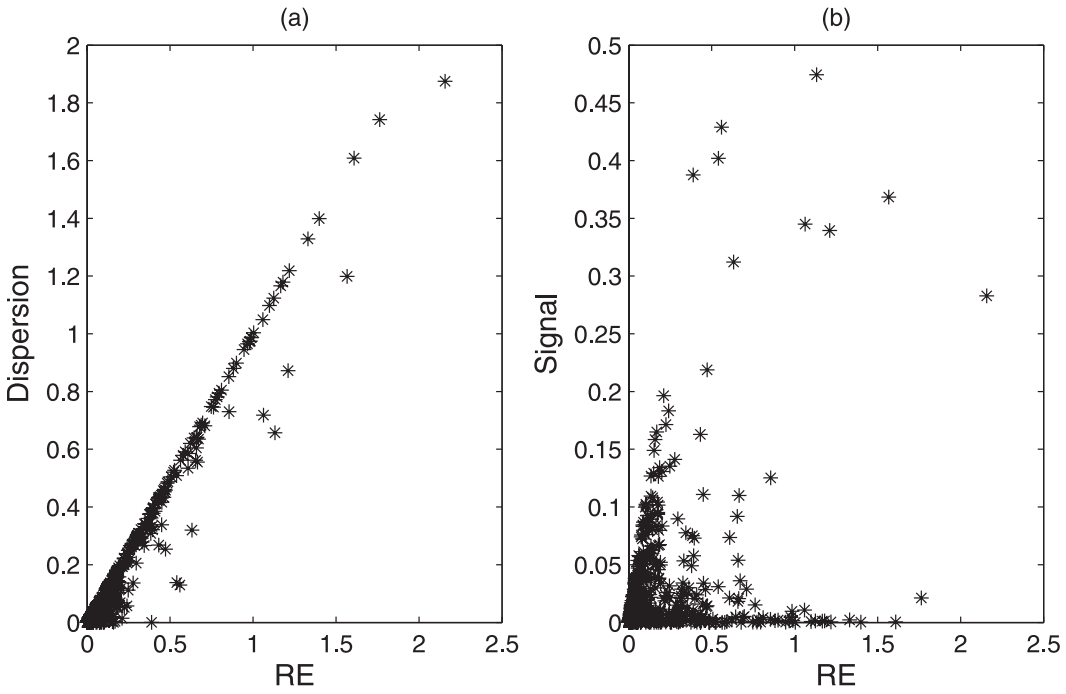

FIG. 15. The relationship of the (a) dispersion component and the (b) signal component to RE.

In this study, we applied the breeding method to a hybrid coupled model and demonstrated the feasibility of using BVs to facilitate ENSO predictability studies. Specifically we performed, for the first time, each BV starting from a realistic ENSO background for the past 120 yr from 1881 to 2000. Meanwhile, retrospective forecasts of the past 120 yr were also conducted. The absence of stochastic atmospheric transients in this hybrid coupled model facilitated the ability of the breeding method to identify slowly growing error modes. The results show that the breeding method was able to detect climatically relevant coupled instabilities present in this coupled model.

The characteristics of ENSO BVs and BV rates were analyzed. It was found that the preliminary BV mode had an ENSO-like structure with a dipole zonal structure between the western Pacific and the eastern Pacific in the subsurface heat content field and a large-amplitude signal in the equatorial central and eastern Pacific. This structure is similar to the final pattern responding to the first singular vector and also reminiscent of the physical processes controlled by the delayed-oscillator mechanism. The dominant structure is insensitive to initial conditions like singular vectors in many ENSO models. However, the spatial structure of each individual BV is sensitive to the initial conditions.

The seasonal dependence of the error growth rate (BV rate) was investigated. The largest BV rates occurred when the model runs through the boreal spring and summer (i.e., spring barrier). The BV rate was also strongly dependent on the ENSO phase. A small error growth rate occurred during the peak ENSO stages, whereas a large error growth rate occurred during the neutral stages. A significant converse relationship existed between the signal of the background SSTA and the error growth rate: the stronger the background SSTA of ENSO, the smaller the BV rate, and vice versa. This converse relationship is primarily due to the nonlinear relationship (e.g., exponential) between the signal and growth rate, as indicated by theoretical analyses (CKT03; Zhou et al. 2007).

To explore ENSO predictability, we conducted retrospective ENSO predictions for the period from 1881 to 2000. The BV rate was analyzed in terms of its ability to measure the model prediction skill. It was found that an overall relationship between the BV rate and prediction skill was absent in this model. Furthermore, we calculated and analyzed the relative entropy from BVs. The relative entropy was found to be an effective indicator of prediction utility. The relationship between the relative entropy and prediction skill varies at a variety of time scales. For individual cases, it appeared to be like a ''triangular relationship'': large relative entropy often led to a good prediction skill; however, when the relative entropy was small, the prediction skill seemed much more variable. At decadal/interdecadal scales, there was consistent variation in prediction skill and in relative entropy. In the late-nineteenth and the late-twentieth

centuries, the relative entropy was large and the model had a high correlation and low RMSE. During other periods, the relative entropy was small, and the model showed the poor prediction skill. Furthermore, it was found that relative entropy was dominated by the spread of BVs, whereas the mean of BVs had little contribution to RE.

The coupled model used in this study was a hybrid coupled in absence of the fastest-growth weather instabilities inherent to stochastic atmospheric transients. While such a hybrid model facilitates the detection of ENSO error modes by using the breeding method, it lacks some necessary physical and dynamical processes that exist in the real world. It would be interesting to validate the results presented in this study with complicated GCM models, a line of research that we will pursue in the future. In addition, the window length of 20 yr used in this study is slightly arbitrary and was motivated by previous work (e.g., Chen et al. 2004; Tang et al. 2008a). Nevertheless, this study analyzed ENSO BVs using realistic ENSO backgrounds as reference trajectories, and, in particular, explored the relationship between BVs and actual prediction skill for a long period of over 100 yr. The results offer valuable insight to ENSO predictability and have practical significance to ensemble prediction.

Acknowledgments. This work is supported by the Canadian Foundation for Climate and Atmospheric Sciences (CFCAS) through Grant GR-7027 and the Canada Research Chair program. We thank the anonymous reviewers for their constructive comments, which helped to improve this manuscript.

REFERENCES

Battisti, D. S., 1988: Dynamics and thermodynamics of a warming event in a coupled tropical atmosphere-ocean model. *J. Atmos. Sci.,* **45,** 2889–2919.

Buizza, R., and T. N. Palmer, 1998: Impact of ensemble size on ensemble prediction. *Mon. Wea. Rev.,* **126,** 2503–2518.

Cai, M., E. Kalnay, and Z. Toth, 2003: Bred vectors of the Zebiak–Cane model and their application to ENSO predictions. *J. Climate,* **16,** 40–56.

Chen, D., M. A. Cane, A. Kaplan, S. E. Zebiak, and D. Huang, 2004: Predictability of El Niño in the past 148 years. *Nature,* **428,** 733–736.

Chen, Y.-Q., D. S. Battisti, T. N. Palmer, J. Barsugli, and E. S. Sarachik, 1997: A study of the predictability of tropical Pacific SST in a coupled atmosphere–ocean model using singular vector analysis: The role of the annual cycle and the ENSO cycle. *Mon. Wea. Rev.,* **125,** 831–845.

Cheng, Y., Y. Tang, X. Zhou, P. Jackson, and D. Chen, 2010: Further analysis of singular vector and ENSO predictability in the Lamont model—Part I: Singular vector and the control factors. *Climate Dyn.,* **35,** 807–826, doi:10.1007/s00382-009-0595-7.

Corazza, M., E. Kalnay, D. J. Patil, S. C. Yang, and R. Morss, 2003: Use of the breeding technique to estimate the structure of the analysis "error of the day." *Nonlinear Processes Geophys.,* **10,** 1–11.

Cover, T. M., and J. A. Thomas, 1991: *Elements of Information Theory*. Wiley, 576 pp.

DelSole, T., 2004: Predictability and information theory. Part I: Measures of predictability. *J. Atmos. Sci.,* **61,** 2425–2440.

——, 2005: Predictability and information theory. Part II: Imperfect forecasts. *J. Atmos. Sci.,* **62,** 3368–3381.

Deng, Z., and Y. Tang, 2009: Reconstructing the past wind stresses over the tropical Pacific Ocean from 1875 to 1947. *J. Appl. Meteor. Climatol.,* **48,** 1181–1198.

——, ——, and X. Zhou, 2008: The retrospective prediction of El Niño–Southern Oscillation from 1881 to 2000 by a hybrid coupled model: (I) Sea surface temperature assimilation with ensemble Kalman filter. *Climate Dyn.,* **32,** 397–413, doi:10.1007/s00382-008-0399-1.

Evensen, G., 2003: The ensemble Kalman filter: Theoretical formulation and practical implementation. *Ocean Dyn.,* **53,** 343–367.

Fan, Y., M. R. Allen, D. L. T. Anderson, and M. A. Balmaseda, 2000: How predictability depends on the nature of uncertainty in initial conditions in a coupled model of ENSO. *J. Climate,* **13,** 3298–3313.

Farrell, B., 1990: Small error dynamics and the predictability of atmospheric flows. *J. Atmos. Sci.,* **47,** 2409–2416.

Goddard, L., S. J. Mason, S. E. Zebiak, C. F. Ropelewski, R. Basher, and M. A. Cane, 2001: Current approaches to seasonal-to-interannual climate predictions. *Int. J. Climatol.,* **21** (9), 1111–1152.

Jin, F.-F., 1997: An equatorial ocean recharge paradigm for ENSO. Part I: Conceptual model. *J. Atmos. Sci.,* **54,** 811–829.

Kalnay, E., 2003: *Atmospheric Modeling, Data Assimilation, and Predictability*. Cambridge University Press, 341 pp.

Kleeman, R., 2002: Measuring dynamical prediction utility using relative entropy. *J. Atmos. Sci.,* **59,** 2057–2072.

——, 2008: Limits, variability, and general behavior of statistical predictability of the midlatitude atmosphere. *J. Atmos. Sci.,* **65,** 263–275.

Lorenz, E. N., 1965: A study of the predictability of a 28-variable atmospheric model. *Tellus,* **17,** 321–333.

Moore, A. M., and R. Kleeman, 1996: The dynamics of error growth and predictability in a coupled model of ENSO. *Quart. J. Roy. Meteor. Soc.,* **122,** 1405–1446.

——, and ——, 1997a: The singular vectors of a coupled ocean-atmosphere model of ENSO. Part I: Thermodynamics, energetics and error growth. *Quart. J. Roy. Meteor. Soc.,* **123,** 953–981.

——, and ——, 1997b: The singular vectors of a coupled ocean-atmosphere model of ENSO. Part II: Sensitivity studies and dynamical interpretation. *Quart. J. Roy. Meteor. Soc.,* **123,** 983–1006.

——, and ——, 1998: Skill assessment for ENSO using ensemble prediction. *Quart. J. Roy. Meteor. Soc.,* **124,** 557–584.

Orrell, D., 2003: Model error and predictability over different timescales in the Lorenz '96 systems. *J. Atmos. Sci.,* **60,** 2219–2228.

Peña, M., and E. Kalnay, 2004: Separating fast and slow modes in coupled chaotic systems. *Nonlinear Processes Geophys.,* **11,** 319–327.

Schneider, T., and S. M. Griffies, 1999: A conceptual framework for predictability studies. *J. Climate,* **12,** 3133–3155.

Smith, T. M., and R. W. Reynolds, 2004: Improved extended reconstruction of SST (1854–1997). *J. Climate,* **17,** 2466–2477.

Suarez, M. J., and P. S. Schopf, 1988: A delayed action oscillator for ENSO. *J. Atmos. Sci.,* **45,** 3283–3287.

Tang, Y., 2002: Hybrid coupled models of the tropical Pacific—Interannual variability. *Climate Dyn.,* **19,** 331–342.

——, and Z. Deng, 2010: Low-dimensional nonlinearity of ENSO and its impact on predictability. *Physica D,* **239,** 258–268.

——, R. Kleeman, and A. M. Moore, 2005: On the reliability of ENSO dynamical predictions. *J. Atmos. Sci.,* **62,** 1770–1791.

——, ——, and S. Miller, 2006: ENSO predictability of a fully coupled GCM model using singular vector analysis. *J. Climate,* **19,** 3361–3377.

——, Z. Deng, X. Zhou, Y. Cheng, and D. Chen, 2008a: Interdecadal variation of ENSO predictability in multiple models. *J. Climate,* **21,** 4811–4833.

——, H. Lin, and A. Moore, 2008b: Measuring the potential predictability of ensemble climate predictions. *J. Geophys. Res.,* **113,** D04108, doi:10.1029/2007JD008804.

Thompson, C. J., 1998: Initial conditions for optimal growth in a coupled ocean-atmosphere model of ENSO. *J. Atmos. Sci.,* **55,** 537–557.

Tippett, M. K., R. Kleeman, and Y. Tang, 2004: Measuring the potential utility of seasonal climate predictions. *Geophys. Res. Lett.,* **31,** L22201, doi:10.1029/2004GL021575.

Toth, Z., and E. Kalnay, 1993: Ensemble forecasting at NMC—The generation of perturbations. *Bull. Amer. Meteor. Soc.,* **74,** 2317–2330.

——, and ——, 1997: Ensemble forecasting at NCEP and the breeding method. *Mon. Wea. Rev.,* **125,** 3297–3319.

Xue, Y., M. A. Cane, and S. E. Zebiak, 1997a: Predictability of a coupled model of ENSO using singular vector analysis. Part I: Optimal growth in seasonal background and ENSO cycle. *Mon. Wea. Rev.,* **125,** 2043–2056.

——, ——, ——, and T. N. Palmer, 1997b: Predictability of a coupled model of ENSO using singular vector analysis. Part II: Optimal growth and forecast skill. *Mon. Wea. Rev.,* **125,** 2057–2073.

Yang, S.-C., M. Cai, E. Kalnay, M. Rienecker, G. Yuan, and Z. Toth, 2006: ENSO bred vectors in coupled ocean–atmosphere general circulation models. *J. Climate,* **19,** 1422–1436.

Young, R. M. B., and P. L. Read, 2008: Breeding and predictability in the baroclinic rotating annulus using a perfect model. *Nonlinear Processes Geophys.,* **15,** 469–487.

Zebiak, S. E., and M. A. Cane, 1987: A model El Niño–Southern Oscillation. *Mon. Wea. Rev.,* **115,** 2262–2278.

Zhou, X., Y. Tang, and Z. Deng, 2007: The impact of atmospheric nonlinearities on the fastest growth of ENSO prediction error. *Climate Dyn.,* **30,** 519–531, doi:10.1007/s00382-007-0302-5.